

The Role of Differential Diffusion during Early Flame Kernel Development under Engine Conditions - Part I: Analysis of the Heat-Release-Rate Response

Tobias Falkenstein^a, Aleksandra Rezchikova^a, Raymond Langer^a, Mathis Bode^a, Seongwon Kang^b, Heinz Pitsch^{a,*}

^a*Institute for Combustion Technology, RWTH Aachen University, 52056 Aachen, Germany*

^b*Department of Mechanical Engineering, Sogang University, Seoul 121-742, Republic of Korea*

Abstract

Although experimental evidence for the correlation between early flame kernel development and cycle-to-cycle variations (CCV) in spark ignition (SI) engines was provided long ago, there is still a lack of fundamental understanding of early flame/turbulence interactions, and accurate models for full engine simulations do not exist. Since the flame kernel is initiated with small size, i.e. with large positive curvature, differential diffusion is expected to severely alter early flame growth in non-unity-Lewis-number ($Le \neq 1$) mixtures as typically used in engines. In this work, a DNS database of developing iso-octane/air flame kernels and planar flames has been established with flame conditions representative for stoichiometric engine part-load operation. Differential diffusion effects on the global heat release rate are analyzed by relating the present findings to equivalent flames computed in the $Le = 1$

*Corresponding author

Email address: office@itv.rwth-aachen.de (Heinz Pitsch)

limit. It is shown that in the early kernel development phase, the normal propagation velocity is significantly reduced with detrimental consequences on the global burning rate of the flame kernel. Besides this impact on the overall mass burning rate, the initial production of flame surface area by the normal propagation term in the flame area balance equation is noticeably reduced. By using the optimal estimator concept, it is shown that strong fluctuations in local heat release rate inherent to $Le \neq 1$ flames in the thin reaction zones regime are mainly contained in the parameters local equivalence ratio, enthalpy, and H-radical mass fraction. Differential diffusion couples the evolution of these parameters to the unsteady flame geometry and structure, which is analyzed in Part II of the present study (Falkenstein et al., *Combust. Flame*, 2019).

Keywords: Flame Kernel, Differential Diffusion, Flame Stretch, DNS, Premixed Flame, Spark-Ignition Engine

1. Introduction

Combustion stability is a prerequisite for more efficient spark ignition (SI) engine operation [2, 3] and reduced engine-out emissions [4, 5]. The occurrence of cycle-to-cycle variations (CCV) is mainly attributed to the very early combustion phase [6], which may take up to 30% of the entire combustion duration to oxidize less than 2% of the in-cylinder fuel mass [7]. By using advanced laser-optical diagnostics, the time until the young laminar flame kernel transitions to a turbulent flame (at approx. 1% burned mass) was shown to correlate with CCV [8]. Further, it was found that stretch effects in $Le \neq 1$ mixtures affect the duration until 10% of fuel are consumed, which

correlates with CCV as well. Although differential diffusion effects have been systematically investigated in spherical expanding turbulent flames by several experimental research groups [9–12], limited accessibility of the smallest time- and length scales demands for complementary numerical analyses.

While *flame kernels* developing in turbulent flow fields have been computed in various DNS studies [13–21], differential diffusion effects have been considered mainly in recent years [22–30]. A non-exhaustive list of DNS parameters and flame conditions that have been investigated to date is provided in Tab. S-1 of the supplementary material.

In the early DNS study by Echehki et al. [22], a Lewis number variation was performed for the very first time in a flame kernel configuration. It was found that flame growth is significantly accelerated in a mixture with $Le = 0.53$ compared to $Le = 1$ conditions. More detailed insights were enabled only many years later by increasing computational power and availability of high-performance computing resources. Dunstan and Jenkins [23] investigated the effect of hydrogen enrichment on the development of lean methane/air flame kernels, in analogy to a previous planar-flame study by Hawkes and Chen [31]. The behavior of pure methane/air flames was shown to be similar in both configurations. By contrast, hydrogen enrichment yielded a stronger enhancement of the flame kernel turbulent burning velocity due to the stronger impact of reduced thermal-diffusive stability in presence of higher global stretch rate. Dinesh et al. [27] performed DNS of lean $H_2/CO/air$ (syngas) flame kernels at two Reynolds numbers with $Le = 0.385$ (realistic) and $Le = 1$. At elevated turbulence levels, the significant increase in flame area caused by thermal-diffusive effects observed at

the lower Reynolds number was found to diminish. Differential diffusion was shown to increase the local burning velocity, hence accelerating flame kernel growth, even at the higher Reynolds (and moderate Karlovitz) number. Alqallaf et al. [30] systematically varied the Lewis number ($Le = 0.8, 1.0, 1.2$) in DNS of flame kernel development computed with single-step chemistry to analyze the effect on flame curvature dynamics. Flame propagation was shown to smoothen the flame surface for $Le \geq 1$, while production of both positive and negative curvatures is promoted in mixtures with $Le < 1$.

Extinction of an H_2 /air ignition kernel, i.e. before the critical radius for self-sustaining flame propagation is reached, was studied by Uranakara et al. [28]. A particle-based analysis was utilized to understand the effect of turbulence-enhanced heat loss leading to extinction. Saito et al. [29] performed two-dimensional DNS to study the effect of small-scale turbulence on the ignition of methane/air and n-heptane/air flame kernels. After normalization with the laminar flame and ignition delay times, similar sensitivities to strain were observed for both mixtures.

Regarding DNS studies on *developed* turbulent flames, those which were performed under engine-relevant conditions or those which considered larger hydrocarbon fuel species are particularly relevant for the present work. Savard et al. [32] analyzed effects of pressure on turbulent, slightly lean ($\phi = 0.9$) iso-octane/air flames at different Karlovitz numbers. Laminar chemical reaction pathways primarily contributing to heat release were significantly changed by ambient pressure. It was found that at low pressures of 1 bar, strong variations in heat release were caused by higher sensitivity to curvature due to differential diffusion as compared to 20 bar. Increased Karlovitz numbers

lead to reduced fluctuations in heat release due to enhanced turbulent species transport inside the flame structure.

Aspden et al. [33] computed lean dodecane/air flames for a range of Karlovitz numbers ($Ka = 1-36$) in the thin reaction zones regime. Small-scale turbulent mixing was found to cause significant deviations in reaction rates from laminar flames computed with $Le = 1$ and $Le > 1$, which is in contrast to methane/air flames [34]. In the low-temperature region of the dodecane/air flame structure, reaction rates of fuel and intermediate species were shown to be significantly reduced at elevated Karlovitz numbers, which was attributed to turbulent perturbations of the fuel breakdown. This effect was identified as a distinct feature of heavy-hydrocarbon flames due to the spatial separation of fuel consumption and heat release.

Although significant progress has been made towards more realistic DNS of premixed flames using detailed chemistry, investigations on the behavior of actual road transportation fuels under engine-relevant turbulence and thermodynamic conditions are still very scarce. While few studies on canonical planar flame configurations exist in literature, the role of molecular transport, as well as its interaction with small-scale turbulent mixing and chemistry inside the flame structure of flame kernels has not been studied in a realistic setting. Experimental evidence on the relevance of early flame kernel development for CCV in SI engines and the lack of accurate models suggest to address this gap in literature. To this end, a new DNS database was designed to be representative for SI engine part-load conditions. Systematic parameter variations were conducted that facilitate the isolation of effects related to the small flame kernel size respective of the hydrodynamic length

scales, as well as of differential diffusion effects. The database consists of five different flame configurations, which have been partly analyzed in previous studies as shown in Tab. 1. To systematically approach the complexity of early flame kernel development, the overall analysis has been divided into four parts by sequentially considering unity- and non-unity Lewis number flames, as well as macroscopic and micro-scale effects. Run-to-run variations in the global heat release rate of flame kernels computed in the $Le = 1$ limit were attributed to the effect of flame front/turbulence interactions on flame surface area evolution [35]. In a subsequent study, the investigation of $Le = 1$ flames with different D_0/l_t (ratio of the initial flame diameter and the integral length scale of turbulence) has shown that such variations in the total flame area are caused by stochastic variations in curvature variance due to large-scale turbulent flow motion with characteristic length scales of at least the flame kernel size [36]. The present study consists of two parts, where the $Le > 1$ datasets are analyzed in detail. In the first part, the heat-release-rate response to differential diffusion effects is analyzed based on the integrated chemical source term, which has high practical relevance, and based on the local chemical source term, which is used to identify the governing parameters in $Le \neq 1$ flames in a quantitative fashion. In the second part [1], the coupling between the local mixture state, which determines the local heat release rate, and the flame geometry and structure is established.

The present manuscript is organized as follows. In Sect. 2, the overall analytical approach pursued to explore differential diffusion effects in the present engine-relevant datasets is summarized. A brief overview of the DNS database is provided in Sect. 3. The global and local heat release rates are

Table 1: Flame realizations available in the overall DNS database.

Configuration	D_0/l_t	Number of Cases	
		Le = 1	Le > 1
Engine flame kernel	0.3	2	4
Large flame kernel	2.0	1	
Planar flame	∞	1	1
Reference		[35, 36]	[1], this

analyzed in Sect. 4 and suitable parameters for a reduced representation of differential diffusion phenomena inside the flame structure are proposed.

2. Analytical Approach

To assess the overall combustion process in technical combustion devices (e.g. in SI engines), global parameters are typically of interest, such as the volume-integrated heat release rate or reaction progress variable source term:

$$\overline{\dot{\omega}_c}|_{\Omega} = \frac{1}{V_{\Omega}} \int_{\Omega} \dot{\omega}_c dV. \quad (1)$$

Here, c is a synonym for a reaction progress variable, e.g. a (normalized) temperature or a quantity representative for the major product species. In spark ignition engines, a fast burning rate is desirable mainly for three reasons.

First, thermal efficiency is improved when approaching the limit of constant-volume combustion. Second, reduced residence times of the end gas (e.g. near hot surfaces) achieved by faster arrival of the flame front may reduce knock tendency. Third, an acceleration of the early flame kernel growth shortens the transition time to a fully developed turbulent flame [7, 8]. This makes the young flame less prone to stochastic kernel/flow interactions, which may significantly reduce CCV. However, differential diffusion effects may severely slow down the early flame kernel development for mixtures of common transportation fuels and air with $Le > 1$.

To give a first impression of the impact of differential diffusion under engine conditions, the integrated reaction source term has been evaluated in a stoichiometric iso-octane/air flame kernel DNS dataset, and an equivalent dataset computed in the $Le = 1$ limit. In Fig. 1 it is shown that $Le = 1$ overall leads to a substantially higher burning rate than in case of the realistic engine fuel, despite a 16% lower *unstretched* laminar burning velocity (cf. Tab. 2). To estimate the influence on CCV in actual engines, the laminar-to-turbulent transition time $\tau_{\text{lam-turb}}$ proposed by Schiffmann et al. [8] has been evaluated for both flames. It turns out that the presence of differential diffusion leads to a 31% increase in $\tau_{\text{lam-turb}}$, which may increase CCV in terms of the coefficient of variance of the mean effective pressure (COV_{IMEP}) from 1.8 to 4.9% (cf. Fig. 7 in [8]).

To gain a general understanding of the complex processes inside the flame structure of turbulent flames and enable the derivation of accurate models, it is desirable to identify a suitable reduced representation of the multi-parameter system and to establish a connection to canonical laminar ref-

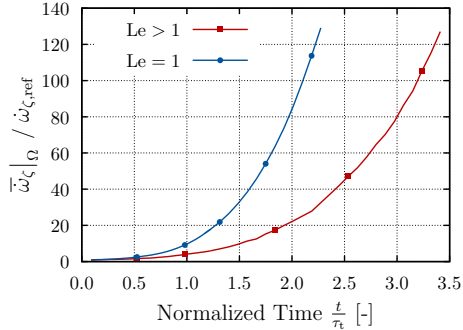


Figure 1: Effect of differential diffusion on the integrated progress variable source term for two equivalent flame kernel DNS datasets.

erence flames. In the present work, this is pursued by following two analysis pathways according to Fig. 2.

Starting point is $\overline{\dot{\omega}_c}|_{\Omega}$ as quantity of interest (QoI) for engine combustion. In a first step, the flames will be considered from a macroscopic perspective that allows to intuitively demonstrate the impact of differential diffusion on early flame kernel development within the frame of the flame surface density (FSD) concept [37]:

$$\overline{\dot{\omega}_c}|_{\Omega} = (\rho s_{l,0}) \cdot \bar{\Gamma}_0 \cdot \bar{\Sigma}_{c,\Omega}, \quad (2)$$

where ρ is the fluid density, $\bar{\Sigma}_{c,\Omega} = \bar{A}_c/V_{\Omega}$ [38] denotes the global flame surface density and the stretch factor $\bar{\Gamma}_0$ quantifies deviations of the displacement speed s_d from the laminar burning velocity $s_{l,0}$ due to ignition, differential diffusion, and turbulent micro-mixing. To parametrize $\overline{\dot{\omega}_c}|_{\Omega}$ entirely in terms of flame structure and geometry, $\bar{\Gamma}_0$ can be decomposed into contributions by normal propagation, which is affected by the flame structure, and by

tangential diffusion, which represents the flame geometry [39]:

$$\begin{aligned}\bar{I}_0 &= \frac{\langle \rho s_d \rangle_{s,\Omega}}{\rho s_{1,0}} = \frac{\langle \rho (s_{rn} - D_{th} \kappa) \rangle_{s,\Omega}}{\rho s_{1,0}} \\ &=: \bar{I}_{0,rn} + \bar{I}_{0,\kappa},\end{aligned}\tag{3}$$

where $\langle \cdot \rangle_s$ denotes generalized scalar-iso-surface averaging [38], s_{rn} is the displacement speed due to reaction and normal diffusion, and D_{th} is the thermal diffusivity. In this work, the mean curvature κ of iso-surfaces belonging to any scalar field ϑ is computed from the normal vector n_i pointing into the direction of negative scalar gradient, i.e. flame kernels have positive global mean curvature:

$$\kappa^{(\vartheta)} = \frac{\partial n_i^{(\vartheta)}}{\partial x_i},\tag{4}$$

$$n_i^{(\vartheta)} = \frac{-1}{|\nabla \vartheta|} \frac{\partial \vartheta}{\partial x_i}.\tag{5}$$

For brevity, the sub/superscript indicating the scalar field will be omitted in most parts below.

The macroscopic perspective based on the reduced flame representation in terms of a propagating front (cf. ① in Fig. 2) enables a separate consideration of differential diffusion effects on $\bar{I}_{0,rn}$ (flame structure and the chemical source term) on the one hand, and on $\bar{I}_{0,\kappa}$ as well as $\bar{\Sigma}_{c,\Omega}$ (flame geometry) on the other hand. In this way, the actual displacement speed of early flame kernels can be related to a laminar unstretched flame and the transition from a quasi-laminar kernel to a fully developed turbulent flame front may be quantified by the evolution of total flame area \bar{A} , which is related to the curvature distribution of the flame [36]. While this perspective already captures the external effect of hydrodynamic strain, a differentiated consideration of energy

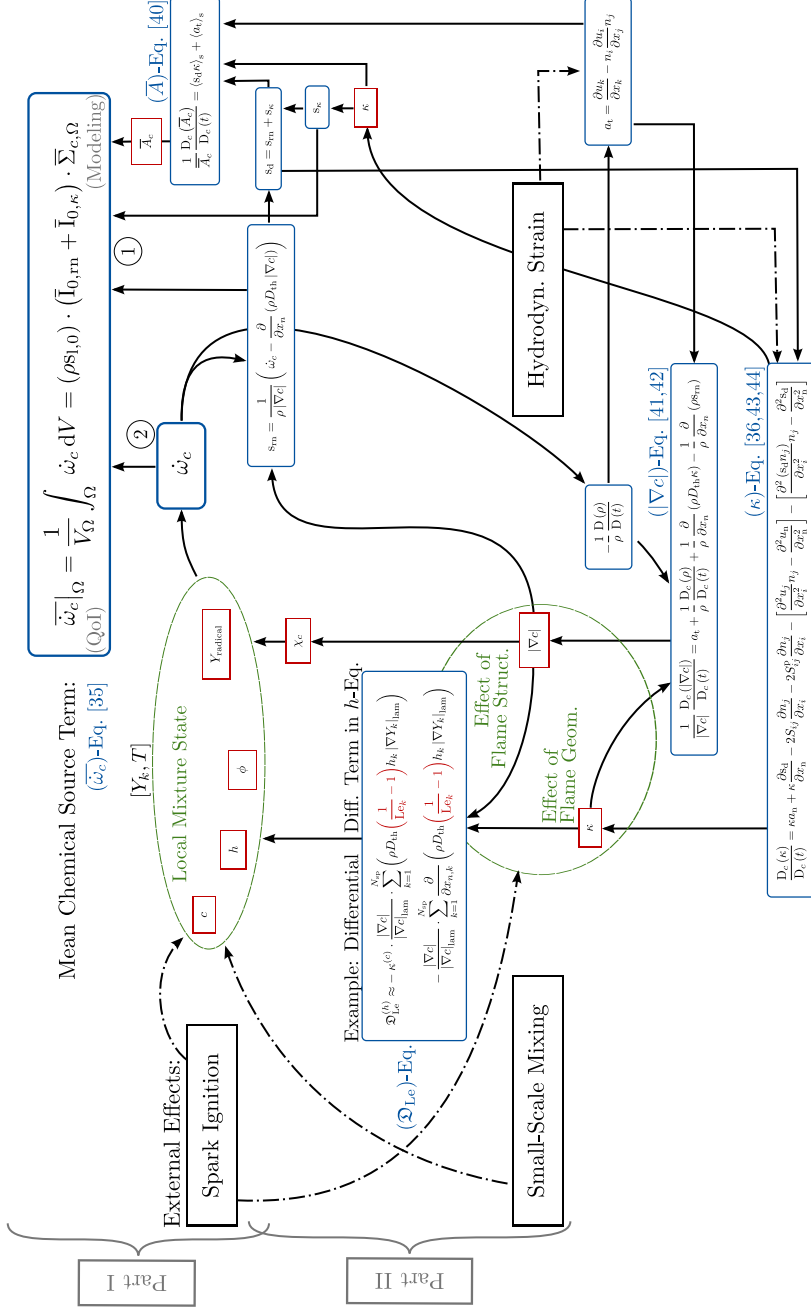


Figure 2: Reduced representation of turbulence/flame interactions on the integrated progress variable source term $\overline{\dot{\omega}_c}$ in presence of differential diffusion ($Le_k \neq 1$). Two analysis pathways are suggested: ① A macroscopic perspective based on the FSD concept (cf. r.h.s. of $(\dot{\omega}_c)$ -Eq. in the blue box) considers a propagating flame front with deviations in flame displacement speed from an unstretched laminar flame, similar to laboratory experiments or classical asymptotic theories [45, 46]. ② A micro-scale perspective on the local source term $\dot{\omega}_c$, which is determined by the local mixture state, characterized by the local equivalence ratio ϕ , enthalpy h , and radical mass fraction Y_{radical} . These parameters change according to the local flame structure ($|\nabla c|$) and geometry (κ), which leads to a response in $\dot{\omega}_c$ to external perturbations of the flame, e.g. by turbulence. In the limit of $Le_k = 1$, ϕ and h remain almost constant across the flame structure, i.e. the coupling between $\dot{\omega}_c$ and $|\nabla c|$ and κ is much weaker than in flames with $Le_k \neq 1$. Note that turbulent fluctuations in the scalar fields ahead of the flame have been omitted.

supply by spark ignition, as well as effects of turbulent micro-mixing on the coupled multi-species system inside the flame structure require an additional analysis pathway.

Starting point for the micro-scale analysis is the local chemical source term $\dot{\omega}_c$ (cf. ② in Fig. 2). In contrast to the displacement speed, the source term only depends on the local state vector $[Y_k, T]$, which shall be expressed first by a reduced parameter set in order to characterize differential diffusion effects. As will be shown in Sect. 4.2, the combination of the local equivalence ratio ϕ , local enthalpy h , and the mass fraction of a radical species is well-suited to capture variations in $\dot{\omega}_c$. While the evolution of each parameter is determined by the respective transport equation, two effects shall be emphasized. First, externally invoked changes in the flame structure ($|\nabla c|$) will lead to modified transport of thermal and chemical internal energy, hence altering the local mixture state. This effect is intrinsic to both $Le > 1$ and $Le = 1$ flames and is here represented by the scalar dissipation rate $\chi_c = 2D_{\text{th}} |\nabla c|^2$. Note that χ_c can be considered as the inverse of a characteristic diffusion time scale [47] and may be used to investigate extinction phenomena, e.g. based on a diffusive Damköhler number [28, 48].

The second significant effect on the local mixture state is limited to flames with $Le_k \neq 1$ and is represented by the (approximate) differential diffusion term \mathfrak{D}_{Le} of the enthalpy equation in Fig. 2. Although the present \mathfrak{D}_{Le} -formulation may not be valid for high-Karlovitz-number conditions, it highlights the importance of local flame structure ($|\nabla c|$) and local geometry (κ) for the occurrence of deviations from laminar flame behavior in case of $Le_k \neq 1$. For more details, refer to Part II of the present study [1]. From the

κ - and $|\nabla c|$ -equations given in Fig. 2, it is immediately obvious that local flame geometry and structure are coupled, i.e. externally invoked changes in κ or $|\nabla c|$ (s_{rn}), e.g. by hydrodynamic strain, may alter the respective other parameter. Overall, the presence of differential diffusion effects ($\text{Le}_k \neq 1$) leads to a response in heat release rate to externally introduced perturbations in local flame geometry and structure, which may in turn change the κ and $|\nabla c|$ balance. Note that in the limit of $\text{Le}_k = 1$, the local mixture state will be much less affected by κ and $|\nabla c|$, i.e. a reduced heat release response to external effects can be expected.

While run-to-run variations between different flame kernel realizations computed in the $\text{Le}_k = 1$ limit were investigated in our previous studies in terms of the $(\overline{\dot{\omega}_c})$ - and (\overline{A}) -Eq. [35] as well as the (κ) -Eq. [36], the objective of the present work is to isolate the effect of differential diffusion on $\overline{\dot{\omega}_c}$ during early flame kernel development. In Part I of the present study, the global heat release rate is first analyzed from the macroscopic perspective (r.h.s. of $(\overline{\dot{\omega}_c})$ -Eq. in Fig. 2) to compare the behavior of a flame kernel computed with a realistic engine fuel to previous results computed in the $\text{Le}_k = 1$ limit. Then, the heat release rate is considered from a micro-scale point of view to identify the parameters that characterize the coupling between $\dot{\omega}_c$ and turbulence/flame interactions in presence of differential diffusion. In Part II of the present study [1], the effect of the local flame structure and geometry on the mixture state (ϕ, h, Y_{H}) and source term $\dot{\omega}_c$ is quantitatively investigated by relating the behavior of flame kernels to corresponding planar turbulent flames and laminar reference solutions.

3. DNS Database

In order to fundamentally characterize early flame kernel development under SI engine conditions, four flame kernel DNS realizations and one planar flame with $Le > 1$ were added to an existing database of three reference flames computed in the $Le = 1$ limit (cf. Tab. 1 and Sect. 3.1). Additional comparative analyses are enabled by laminar unstretched and stretched flamelet solutions, which will be summarized in Sect. 3.2.

3.1. Three-Dimensional DNS

The DNS database has been carefully designed to be representative for SI engine part-load conditions. Since the governing equations and numerical methods were extensively described in our previous study on the same flame configurations as in this work, but with all Lewis numbers artificially set to unity [35, 36], only a brief summary is provided in the following. To enable systematic investigations on differential diffusion effects, four flame kernel realizations and one planar reference flame with realistic (but constant) Lewis numbers have been added to the existing $Le = 1$ database. Hence, four flame configurations (kernel/planar, $Le = 1/Le > 1$) are available for this study. While the flame conditions listed in Tab. 2 are fully equivalent to our previous work [35, 36], some differences in the non-dimensional groups given in Tab. 3 emerge due to the smaller chemical time scale of the laminar unstretched flame with $Le > 1$. In Tab. 2, the mixture thermodynamic state is given by the pressure $p^{(0)}$ and temperature of the unburned gas T_u with equivalence ratio ϕ_u . Note that the turbulent flow field corresponds to decaying homogeneous isotropic turbulence, which explains the DNS param-

Table 2: Flame conditions in the DNS.

Property	Value
Mixture	Iso-Octane/Air
$p^{(0)}$	6 bar
T_u	600 K
ϕ_u	1.0 (homogeneous)
s_1^0	0.73 0.63 m/s
l_f	69.1 71.3 μm
Flow Field	Decaying h.i.t.
Combust. Regime	Thin Rct. Zones
Le_{eff}	2.0 1.0

eter ranges given in Tab. 3. The turbulent integral length scale and eddy turnover time are denoted by l_t and τ_t , η is the Kolmogorov length scale, while the laminar flame thickness and initial flame diameter are referred to as l_f and D_0 , respectively. Due to computational restrictions, the wavenumber range covered by the DNS is smaller than in an actual engine. Hence, the integral length scale in the simulations is two to three times smaller than in reality, while the Karlovitz number is closely matched to actual engine conditions at part load [49]. For an illustration of the DNS conditions in the regime diagram of turbulent combustion and a discussion of the engine relevance of the DNS configuration, refer to [35]. Although the Karlovitz number in that study was slightly higher than in the present work due to the $Le = 1$ simplification, it was shown that no thickening of the averaged flame structure occurs.

In order to quantitatively assess the impact of differential diffusion on the heat release rate, a detailed chemical reaction scheme is required [52]. As in our previous study, a modified kinetic model based on the skeletal iso-octane mechanism by Pitsch and Peters [53] was used. Validation results for the reaction scheme calibrated to the present DNS conditions are provided as supplementary material. Diffusive scalar transport was solved based on the Curtiss-Hirschfelder approximation [54] with additional consideration of the Soret effect (thermodiffusion). With respect to the accuracy of the diffusion model employed here, refer to the work by van Oijen et al. [55], where premixed CH_4/H_2 flame solutions computed with the Curtiss-Hirschfelder approximation and with a complex diffusion model based on the Stefan-Maxwell equations were compared.

Table 3: Engine [50, 51] and DNS characteristic numbers ($Le > 1$).

Parameter	Engine	DNS ($t_{\text{init}} - t_{\text{end}}$)
Re_t	100 – 2390	385 – 222
$\frac{u_{\text{rms}}}{s_1^0}$	2 – 15	5.9 – 2.8
Ka	1 – 6	10.6 – 3.2
Da	1 – 100	1.9 – 4.6
$\frac{l_t}{\eta}$	100 -200	87.2 – 57.2
$\frac{l_t}{l_f}$	20 – 147	10.9 – 13.0
$\frac{D_0}{l_t}$	< 1.0	0.3 ∞

A brief summary of the DNS setup is given in Tab 4. All flames were initialized in the same realization of a decaying homogeneous isotropic turbulent flow field, which was generated from a combination of multiple forced turbulence solutions as described in our previous study [35]. One important difference between the flame kernel datasets and the planar reference flames is the initialization method. Flame kernels were ignited by a source term in the temperature equation, which results in an early growth phase comparable to engine experiments reported in literature (cf. [36]). By contrast, a laminar unstretched flame was imposed into the turbulent flow field as initial condition for the planar-flame DNS to avoid strong dilatation due to the larger burned volume. Multiple flame kernel realizations were computed by initializing each simulation with the same flow field, while varying the

ignition location by more than five integral length scales between simulation runs. To provide flame statistics for the particularly critical early flame kernel development phase and to limit the overall computational costs, one reference flame kernel computed for a physical time of $t_{\text{sim.}} = 3.4 \cdot \tau_t$ has been supplemented by three realizations that were simulated until $t_{\text{sim.}} = 1.0 \cdot \tau_t$ (cf. Tab. 4). The planar flame simulation was stopped after $t_{\text{sim.}} = 2.8 \cdot \tau_t$, which is approximately the time when the flame front can be considered as fully developed based on near-zero total flame area rate-of-change. While flame kernels were computed in an isochoric setting with periodic boundary conditions, an outlet boundary condition was used to achieve isobaric conditions for the planar flame. For the main flame kernel reference case, the pressure increase at $t_{\text{sim.}} = 3.4 \cdot \tau_t$ was below 8.5 %.

To simplify the analysis and make the dataset more accessible for modelling, a new reaction progress variable ζ has been defined by the solution of the transport equation [35]

$$\frac{\partial(\rho\zeta)}{\partial t} + \frac{\partial(\rho u_j \zeta)}{\partial x_j} = \frac{\partial}{\partial x_j} \left(\rho D_{\text{th}} \frac{\partial \zeta}{\partial x_j} \right) + \dot{\omega}_\zeta. \quad (6)$$

The chemical source term was chosen as the sum of source terms of main product species:

$$\dot{\omega}_\zeta = \dot{\omega}_{\text{H}_2} + \dot{\omega}_{\text{H}_2\text{O}} + \dot{\omega}_{\text{CO}} + \dot{\omega}_{\text{CO}_2}. \quad (7)$$

Solving Eq. (6) in the DNS simplifies the analysis of the overall normal and tangential diffusion effects, as compared to a progress variable definition that results in a balance equation with more complex diffusive transport terms. Differences between the r.h.s. of Eq. (6) and the balance equation of a progress variable $c = Y_{\text{H}_2} + Y_{\text{H}_2\text{O}} + Y_{\text{CO}} + Y_{\text{CO}_2}$ are quantitatively discussed in Sect. 3 in

Table 4: Computational setup of the DNS.

Property	Value
Grid Size	960 ³
Domain Size	15 · l_t
Navier-Stokes Eq.	Low-Mach-Approx. [56]
Transport Model	Curt.-H. [54], const.-Le
Soret Effect	yes
Chem. Mechanism	26 Spec., based on [53]
<i>Flame Kernels:</i>	
– Initialization	– Ign. Heat Source
– Boundry. Cond.	– x, y, z -dir.: periodic
– Sim. Time	– 1x ($t_{\text{sim.}} = 3.4 \cdot \tau_t$), – 3x ($t_{\text{sim.}} = 1.0 \cdot \tau_t$)
<i>Planar Flame:</i>	
– Initialization	– Lam. Flamelet
– Boundry. Cond.	– x -dir.: symm./outlet, – y, z -dir.: periodic
– Sim. Time	– ($t_{\text{sim.}} = 2.8 \cdot \tau_t$)

the supplementary material. The decomposition of the first term in the r.h.s of Eq. (6) according to Echehki and Chen [39] will be employed in Sect. 4.1 to analyze the decomposed stretch factor (cf. Eq. (3)).

3.2. Laminar Flame Calculations

To relate local conditions inside the turbulent flame structures to laminar flamelet solutions, several one-dimensional flames were computed with the *FlameMaster* code [57]. Steady, unstretched laminar flames (sub/superscript ‘lam’) were solved based on the algorithm by Smooke et al. [58]. To generate stretched reference flames, the premixed back-to-back counterflow configuration (sub/superscript ‘cff’) has been selected in analogy to previous modeling studies [59, 60]. The numerical solutions were obtained based on the similarity coordinate formulation assuming a potential flow in the far field [61]. For reaction mechanism validation and assessment of early flame kernel growth, laminar spherical flames (sub/superscript ‘sph’) have been computed in Lagrangian coordinates [62] using DASSL [63].

A detailed analysis of the laminar unstretched flame structure in iso-octane/air flames in terms of a very similar kinetic scheme as used in the present study was provided by Pitsch and Peters [53] and is not repeated here. For a discussion of differential diffusion effects on flame structure and extinction in the premixed counterflow configuration, refer to the modeling study by van Oijen and de Goey [64] or the review paper by Lipatnikov and Chomiak [65].

4. Results

As described in Fig. 2, the analysis of heat-release-rate response has been conducted according to two logical pathways. In Sect. 4.1, differential diffusion effects on the *global heat release rate* will be discussed from the macroscopic perspective by considering two equivalent flame kernel datasets computed with $Le > 1$ and $Le = 1$, respectively. For the micro-scale analysis, the ability of several reduced parameter sets to capture differential-diffusion-induced fluctuations in the *local heat release rate* of planar flames will be quantified in Sect. 4.2. The main results will be used to explain the Lewis number effects on the global heat release rate of flame kernels observed in Fig. 1.

4.1. Global Heat Release Rate Evolution

To better understand the strong impact of differential diffusion on $\overline{\dot{\omega}_c}|_{\Omega}$ that was shown in Fig. 1, the stretch factor \bar{I}_0 and the flame surface density $\bar{\Sigma}_{c,\Omega}$ will be considered according to the r.h.s. of the $(\overline{\dot{\omega}_c})$ -Eq. in Fig. 2. In this way, differential diffusion effects on the local burning velocity can be distinguished from effects on flame area evolution. Note that the results in Fig. 1 were plotted as function of time, which is relevant for the engine application. However, this representation implies that differences in the integrated source term accumulate due to growing differences in flame kernel size. In order to rigorously analyze the role of differential diffusion during flame development, it is desirable to enable comparisons of data extracted from flames with similar geometry and size. Hence, results will be shown as function of kernel radius hereafter. The radius R_{50} is here defined as the

median of the distance distribution, measured between all flame points and the geometric center of the flame. It should be noted that at the same flame kernel radius, the flames are exposed to slightly different turbulence intensity since the turbulence decays over time. At a flame radius of one integral length scale $R_{50} = l_t$ (cf. Fig. 1), the turbulent kinetic energy differs by 7%.

A comparison of the stretch factors evaluated for both the $Le > 1$ and the $Le = 1$ turbulent flame kernel is provided in Fig. 3 (a). Initially, \bar{I}_0 is dominated by the effect of spark ignition, which affects the early flame kernels until a radius of approximately one integral length scale is reached. This behavior is similar to actual engines, as discussed in our previous study [36]. At the kernel size of one integral length scale, differential diffusion effects reduce \bar{I}_0 by 33%. This is a stronger reduction than observed for two laminar spherical expanding flames, which were ignited in the same way as the DNS and are plotted in Fig. 3 (a) for reference (superscript ‘sph’). As shown in Part II of the present study [1], turbulence detrimentally alters the flame structure by hydrodynamic strain, in addition to the unfavorable effect of large positive curvature on the heat release rate of $Le > 1$ flame kernels. It should be noted that \bar{I}_0 quantifies the deviation of the actual flame displacement speed from the respective laminar burning velocity, which is in fact lower in case of $Le = 1$ ($s_{l,Le=1}^0/s_{l,Le>1}^0 = 0.84$). At the kernel size of one integral length scale, the net displacement speed of the $Le > 1$ flame is 21% lower than in the $Le = 1$ limit. This is interesting, since the unstretched laminar burning velocity for the $Le > 1$ case is actually larger than for the $Le = 1$ case. Similar findings have also been reported by Savard and Blanquart [66]

who studied n-heptane/air flames both for $Le > 1$ and $Le = 1$.

To gain additional insights, the stretch factor is here decomposed into a component representative of flame normal propagation and a curvature effect (cf. Eq. (3)). Obviously, the normal-propagation stretch factor $\bar{I}_{0, rn}$ is significantly reduced in the $Le > 1$ flame after ignition effects have decayed. According to the (s_{rn}) -Eq. in Fig. 2, this can be due to changes in the chemical source term $\dot{\omega}_c$ and the scalar gradient magnitude $|\nabla c|$, which is related to the local flame thickness. From the definition of $\bar{I}_{0, \kappa}$ (cf. Eq. (3)), it can be expected that differential diffusion only has a minor effect on this term, since the correlation between curvature and the diffusion coefficient is rather weak and mean curvature is not altered by changes in Lewis number. This is confirmed by the results shown in Fig. 3 (a). Note that $\bar{I}_{0, \kappa}$ is a measure for diffusive transport of ζ in iso-surface-tangential directions, while curvature effects on the chemical source term are contained in $\bar{I}_{0, rn}$.

The domain-integrated generalized flame surface density $\bar{\Sigma}_{\zeta, \Omega}$ is plotted in Fig. 3 (b) as function of kernel radius. Obviously, the realistic engine fuel leads to a suppression of net flame area production due to thermal-diffusive effects, which is in agreement with planar flame results reported in literature [67–69]. When the flame kernels have reached a radius of one integral length scale, which corresponds to the time when ignition effects have mostly decayed [36], the flame surface density of the $Le > 1$ flame is reduced by 15% compared to the $Le = 1$ case. Note that both turbulent flames exhibit significantly larger surface areas than a perfect sphere with the same radius, as indicated in the figure. From the preceding discussion it can be concluded that the reduction in integral heat release rate attributed

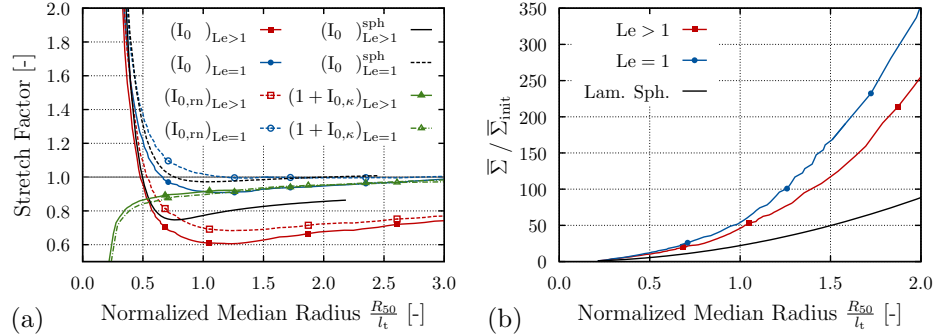


Figure 3: Flame Kernel: Mean stretch factor (a) and domain-integrated generalized flame surface density (b) as function of kernel radius. Superscript ‘sph’ corresponds to a laminar spherical expanding flame.

to differential diffusion effects is initially dominated by the burning velocity, while noticeable differences in flame area exist as well.

In order to further investigate how differential diffusion reduces the overall flame surface area (or $\bar{\Sigma}_{\zeta,\Omega}$) and consequently the integral heat release rate of the $Le > 1$ flame kernel (cf. Fig. 3 (b)), the total flame area rate-of-change is considered [35]:

$$\frac{1}{\bar{A}_{\zeta,\Omega}} \frac{D_{\zeta}}{D_{\zeta}(t)} (\bar{A}_{\zeta,\Omega}) = \frac{\int_{\Omega} ((s_{rn}\kappa) - D_{th}\kappa^2 + a_t) |\nabla\zeta| dV}{\int_{\Omega} |\nabla\zeta| dV}. \quad (8)$$

Results extracted from the $Le > 1$ and the $Le = 1$ datasets are compared as function of kernel size in Fig. 4. First, we focus on the evolution of the l.h.s. of Eq. (8) to assess differences in net area rate-of-change. As shown in Fig. 4 (a), flame area production is overall positive due to the presence of mean flame curvature, but generally higher in the $Le = 1$ case. At ($R_{50} = 1.0 \cdot l_t$), when ignition effects have mostly decayed, differential diffusion leads to a reduction in flame area production rate by 25%. From the strong reduction in flame normal-propagation velocity observed in Fig. 3 (a), it can be expected that

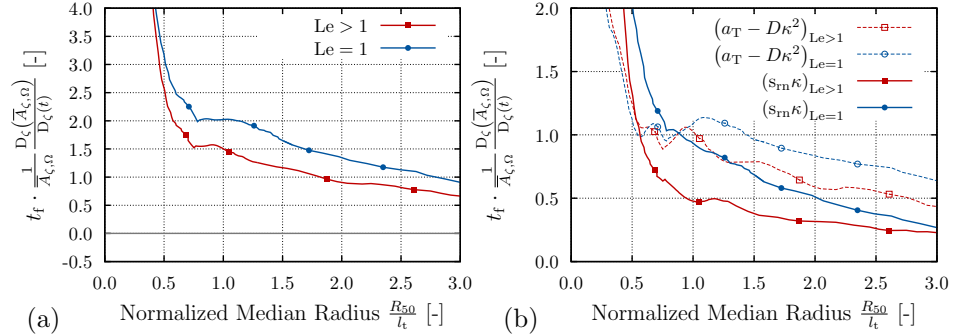


Figure 4: Flame kernel area rate-of-change as function of kernel radius: Net effect (a), contribution by normal propagation shown separately (b).

the first term in the r.h.s. of Eq. (8), i.e. the change in flame area due to normal propagation of a curved surface, plays a major role in causing this difference. Hence, this term is plotted separately from the tangential strain and scalar dissipation terms in Fig. 4(b). In this way, it becomes obvious that the normal-propagation term is responsible for almost all differences in early flame area growth in the range ($R_{50} < 1.0 \cdot l_t$). In particular, the sum of the remaining two terms is initially very similar for both Lewis number cases, while differential diffusion reduces the area production through normal propagation by up to 50%. During this early phase, the effect of differential diffusion on flame kernel area growth may be similar to laminar flames (cf. Fig. 3(a)). As the flame kernels grow in size, differences in the curvature distributions develop (cf. Part II [1]), which cause differences in heat release rate that feed back into the tangential strain term in Eq. (8).

The preceding discussion has shown that differential diffusion has a strong impact on the burning rate during flame kernel development under engine-relevant conditions especially because of its influence on flame normal propa-

gation. Both flame area and flame displacement speed are significantly lower in the flame computed with a realistic transportation fuel, i.e. with $Le > 1$. Compared to an unstretched laminar flame, the net displacement speed is reduced by up to 40% due to differential and tangential diffusion. As this minimum in displacement speed occurs at very small flame radii, the overall flame kernel behavior may still be very sensitive to stochastic interactions with the turbulent flow field [36]. Hence, the discussed burning-rate evolution is expected to be particularly critical for the occurrence of CCV in SI engines.

4.2. Local Heat Release Rate Variations

To further investigate the strong Lewis-number dependence of the mean normal-propagation stretch factor $\bar{\Gamma}_{0,m}$ (cf. Sect. 4.1), the parameter interactions inside the flame structure that govern the local heat release rate will be analyzed in the following. Since the physical and chemical phenomena inside an unsteady flame structure are already quite complex, the following analysis is simplified by limiting ourselves to the fully developed, statistically planar-turbulent-flame datasets. Most importantly, the planar flame configuration provides sufficient statistics for a rigorous comparison between the $Le > 1$ and the $Le = 1$ cases. It will be shown that in addition to a reduction in mean heat release rate, tremendous fluctuations in heat release rate exist throughout the flame structure of the $Le > 1$ flame. To parametrize the heat release rate in $Le \neq 1$ flames, the combination of local equivalence ratio, enthalpy, and radical availability will be quantitatively compared to other parameter choices and confirmed as suitable parameter set, in agreement with individual findings from literature that were used to design Fig. 2.

To get a first impression of the impact of differential diffusion on the spatial heat release distribution, the temperature iso-surfaces corresponding to maximum heat release rate in the laminar unstretched flame (T_{maxHR}) have been extracted from both planar-turbulent-flame datasets at $t = 2.8 \tau_t$ and are colored by heat release rate in Fig. 5. In the $Le = 1$ dataset, the heat release rate distribution is almost uniform. This already suggests that in the $Le = 1$ limit, the coupling of χ_c and $\dot{\omega}_c$ (cf. Fig. 2) does not lead to significant spatial variations in $\dot{\omega}_c$ under the present flow conditions. Conversely, the more engine-relevant flame with $Le > 1$ features similarly high source term magnitudes only in regions of negative curvature, while large parts of the plotted iso-surface exhibit significantly reduced heat release rates. This observation is consistent with the correlation between the fuel consumption rate and curvature that was previously shown for an n-heptane/air flame in the broken reaction zones regime [66] and the correlation between the consumption speed and curvature in $Le \neq 1$ flames located in the corrugated flamelet regime [67]. Correlations between the local heat release rate and flame structure/geometry are discussed in Part II of the present study [1]. For a visualization of differential diffusion effects during flame kernel development, refer to Figs. S-6 and S-7 of the supplementary material.

To enable a more quantitative understanding of differential diffusion effects on the heat release rate distribution across the flame structure, joint-PDFs of heat release rate and temperature are shown in Fig. 6. Additionally, conditional mean results are plotted for comparison with laminar reference data. In the $Le = 1$ flame, the heat release rate of an unstretched premixed flame is almost perfectly recovered (cf. Fig. 6(a)). In

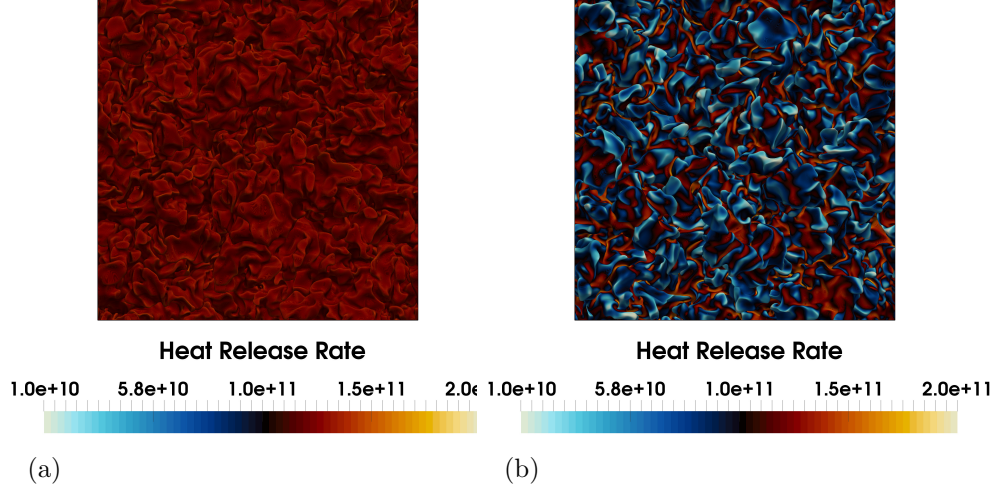


Figure 5: Planar Flame: $T_{\max\text{HR}}$ iso-surface colored by local heat release rate for the $\text{Le} = 1$ dataset (a) and the engine-relevant $\text{Le} > 1$ flame (b) at $t = 2.8 \tau_t$.

the $\text{Le} > 1$ case, a different behavior is expected due to the reduction in stretch factor that was observed in the corresponding flame kernel dataset (cf. Fig. 3(a)). As shown in Fig. 6(b), the maximum conditional mean heat release rate of the turbulent planar flame is reduced by 29 % with respect to the laminar unstretched value. A very similar reduction was observed by Savard et al. [32] for a slightly lean iso-octane/air flame with comparable Karlovitz number, but computed at a higher pressure and temperature of 20 bar and 800 K. For reference, data extracted from a back-to-back counterflow flame (c.f.f.) solution has been added to the plots in Fig. 6. The strained laminar flame solutions have been selected based on the condition $|\nabla T|_{\max\text{HR},\text{eff}} = \langle |\nabla T| \mid (T = T_{\max\text{HR}}, \kappa = 0) \rangle$ and will be analyzed in more detail in Part II [1]. Note that in the $\text{Le} = 1$ limit (cf. Fig. 6(a)), the effect of χ_c on the mixture state sketched in Fig. 2 seems to be small under the

present flow conditions. The $Le > 1$ flame additionally exhibits a heat release rate dependence on curvature, which also explains the difference between the turbulent and the laminar profiles on the high-temperature side of the peak in Fig. 6 (b).

Besides the reduction in mean heat release rate observed in the planar, $Le > 1$ flame as compared to the corresponding $Le = 1$ dataset, visual inspection of Fig. 6 immediately suggests a strong impact of differential diffusion on variations in local heat release rate. While the data points in the $Le = 1$ case shown in Fig. 6(a) are distributed in a rather narrow band around the conditional mean profile, tremendous scatter from almost extinguished flamelets to levels well above the unstretched reference flame is present in the $Le > 1$ dataset. Note that the occurrence of flame elements with particularly low heat release rates was previously identified as a distinct feature of the thin reaction zones regime [70]. Here, temperature rather than the progress variable ζ was chosen as independent variable for this analysis to facilitate comparisons with other studies [32, 66, 71]. Joint-PDFs of $\dot{\omega}_\zeta$ and ζ are provided in Fig. S-4 in the supplementary material. The preceding discussion on the planar flame datasets is additionally supported by qualitatively similar results for the flame kernel configuration provided in Fig. S-5 in the supplementary material.

As a next step, we seek to identify the parameters that govern the local heat-release-rate response to differential diffusion effects, i.e. the observed *high conditional variance* and *reduced conditional mean*. The findings will be used to relate the detrimental reduction in global heat release rate due to $Le > 1$ (cf. Fig. 1) to the mixture conditions inside the flame structure. To

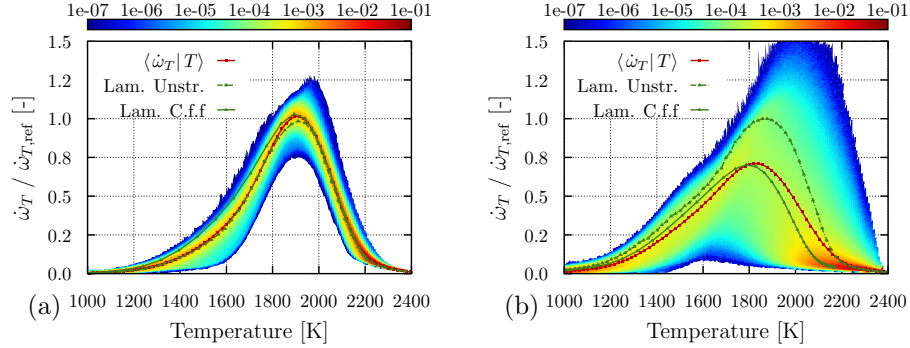


Figure 6: Planar Flame: Joint-PDFs of heat release rate and temperature for the $Le = 1$ dataset (a) and the engine-relevant $Le > 1$ flame (b) at $t = 2.8 \tau_t$. Similar results are shown for the flame kernel configuration in Fig. S-5 in the supplementary material

this end, we make use of the optimal estimator analysis technique [72, 73]. The primary objective of the following parameter tests is not to derive or check a specific model, but to quantify the ability of a selected input parameter set to predict local heat release rate throughout the flame structure, irrespective of a functional model expression. In this regard, the optimal estimator concept is a powerful tool which is based on two main ideas. First, the conditional mean of a dataset is considered as an ideal reference model, i.e. the optimal estimator. Second, the expected error of a model based on the selected input parameters Π cannot be smaller than the standard deviation from the respective optimal estimator, which is cast into an error measure called the irreducible error:

$$\epsilon^2(\Pi) = \left\| [\dot{\omega}_T - \|\dot{\omega}_T | \Pi\|]^2 | \Pi \right\|. \quad (9)$$

To reduce fitting errors which may pollute the optimal estimator results, artificial neural networks have been employed as suggested by Berger et al. [74]. Since we are specifically interested in the role of differential dif-

fusion, all irreducible errors have been normalized by $\epsilon_{\text{Le}=1}^2(T)$, i.e. the error value computed for the $\text{Le} = 1$ flame when using temperature as the only model parameter. Hence, a normalized error value of unity would imply that the scatter around the conditional mean yields the same error sum as computed from the data points plotted in Fig. 6 (a). The expected irreducible errors associated to heat release rate predictions from different input parameter sets in the $\text{Le} > 1$ flame are listed in Tab. 5. When only temperature is used to parametrize heat release rate (cf. Fig. 6 (b)), the irreducible error is 5.5 times larger than in the $\text{Le} = 1$ flame.

The empirical input parameter selection closely follows the schematic shown in Fig. 2 in a backward-analysis fashion, starting from the local heat release rate $\dot{\omega}_T$ as quantity of interest. From a chemical kinetic point of view it might be interesting to begin the backward analysis with the identification of pathways that differ between the $\text{Le} > 1$ and the $\text{Le} = 1$ flames. Similar analyses have been published for different fuels [75, 76], including systematic variations of the Lewis number [71], but are not pursued here. Still, finding suitable marker species which contain most of the observed heat release rate variations may serve as a starting point for future work and may suggest control variables for flamelet modeling. Due to the direct influence of individual species mass fractions on chemical source terms, these are here referred to as *first-level parameters* (reaction/diffusion-controlled). Among common marker species used for modeling of hydrocarbon flames [59], molecular hydrogen was found to yield an irreducible error $\epsilon^2(T, Y_{\text{H}_2})$ comparable to the reference error $\epsilon_{\text{Le}=1}^2(T)$. The selection of suitable marker species candidates will be further discussed below.

As a next step, heat release rate has been parametrized by the stoichiometry and energy content of the local mixture. The chosen *second-level parameters* (diffusion-controlled) for a reduced representation of the mixture state are local equivalence ratio [77, 78] and enthalpy [79], which are not changed by chemical source terms. The local equivalence ratio ϕ is defined by

$$\phi = \frac{2 \mathfrak{X}_{\text{C}} + 0.5 \mathfrak{X}_{\text{H}}}{\mathfrak{X}_{\text{O}}}; \quad \mathfrak{X}_{\ell} = \sum_{k=1}^{N_{\text{sp}}} a_{k,\ell} X_k, \quad (10)$$

where \mathfrak{X}_{ℓ} denotes the element mole fraction of element ℓ , X_k is the mole fraction of species k , and $a_{k,\ell}$ is the number of atoms of element ℓ contained in a molecule of species k [78]. Recall that the unburned mixture is homogeneous, i.e. variations in both parameters can only occur due to differential and thermodiffusion. Although enthalpy and equivalence ratio are not independent quantities [64], $\epsilon^2(T, \phi, h)$ is clearly beneficial compared to using only one of both parameters. Note that the irreducible error $\epsilon^2(T, h)$ is larger than $\epsilon^2(T, \phi)$, which seems in contradiction to the early work by Ashurst et al. [79], who identified enthalpy as a suitable parameter to characterize flame dynamics in $\text{Le} \neq 1$ mixtures. This discrepancy to the present results is likely a feature of the multi-species system as opposed to single-step-chemistry DNS. The irreducible error can be further reduced by supplementing the second-level parameter set by one radical mass fraction [10, 80, 81]. In particular, $\epsilon^2(T, \phi, h, Y_{\text{H}})$ yields the smallest normalized error value of all $\text{Le} > 1$ tests. In fact, this parameter set gives the same errors in both the $\text{Le} > 1$ and $\text{Le} = 1$ flames, which is in agreement with the combination of individual findings reported in literature (cf. Fig. 2). Although molecular hydrogen was identified as the most suitable first-level-parameter, the com-

bination $(T, \phi, h, Y_{\text{H}_2})$ is less effective than considering radical availability, which is due to a strong correlation between Y_{H_2} and ϕ as indicated by the almost identical irreducible errors for (T, Y_{H_2}) and (T, ϕ) . This observation is supported by the joint-PDF of ϕ and Y_{H_2} for a given temperature and Y_{H} as shown in Fig. A.1 (a).

As enthalpy and equivalence ratio variations are linked to flame curvature and scalar gradient magnitudes through \mathfrak{D}_{Le} (cf. Fig. 2), κ and $|\nabla T|$ form the *third-level parameters* (kinematic) for a reduced description of the flame geometry and structure. For simplicity, only the temperature field has been considered to evaluate both parameters, which is a reasonable approximation in the present datasets (cf. Part II [1]). However, the approximate expression for \mathfrak{D}_{Le} given in Fig. 2 is certainly inexact and will result in an increased irreducible error. While accounting for curvature in $\epsilon^2(T, \kappa)$ leads to some reduction in the expected irreducible error, the dominant third-level parameter seems to be $|\nabla T|$. Note that $|\nabla T|$ may affect the mixture state through \mathfrak{D}_{Le} and χ as sketched in Fig. 2. Although $|\nabla T|$ and κ are not independent [82], the parameter combination yields a lower error $\epsilon^2(T, \kappa, |\nabla T|)$, which is still more than 50% higher than the reference error $\epsilon_{\text{Le}=1}^2(T)$. It should be noted that such deterioration in performance of an ideal model is expected as the relation between the quantity of interest (heat release rate) and input parameters becomes weaker. This increased variance compared to the $\text{Le} = 1$ flame might be due to local changes in species mass fractions and gradients induced by turbulent micro-mixing (i.e. the temperature field may be less representative) or finite response time of the second-level (diffusion-controlled) parameters (ϕ, h) to changes in curvature and scalar gradients.

The latter effect is investigated by testing a *fourth-level parameter set* (kinematic/dynamic), which contains an additional quantity representative for the time rate-of-change of the third-level parameters. Here, the tangential strain rate has been selected as a measure for hydrodynamic changes to the flame structure (cf. $(|\nabla T|)$ -Eq. in Fig. 2) and geometry. In fact, a correlation between local enthalpy and strain rate was already shown to exist in the earliest DNS with $Le \neq 1$ [79]. Since it is well-known that curvature and strain are correlated [67, 83], it is not surprising that the irreducible errors $\epsilon^2(T, |\nabla T|, a_t)$ and $\epsilon^2(T, |\nabla T|, \kappa)$ are identical. Still, accounting for both curvature and tangential strain in addition to $|\nabla T|$ is even more effective. An almost identical irreducible error is achieved by replacing the tangential strain rate by the gradient rate-of-change (l.h.s. of $(|\nabla T|)$ -Eq. in Fig. 2) to include the flame structure dynamics into $\epsilon^2\left(T, \kappa, |\nabla T|, \frac{1}{|\nabla T|} \frac{D_T(|\nabla T|)}{D_T(t)}\right)$.

The optimal estimator analysis has quantitatively shown that at a given progress variable (temperature), preferential diffusion effects on the heat release rate are well represented by the parameter set (ϕ, h, Y_H) . To illustrate this finding, the data that was shown in Fig. 6 (a,b) has been additionally conditioned on $(\langle \phi | T \rangle, \langle h | T \rangle, \langle Y_H | T \rangle)$ for each flame, i.e. at a given temperature, all points share the same mixture state characterized by (ϕ, h, Y_H) . As shown in Fig 7, the remaining scatter around the conditional mean heat release rate is similar for both $Le > 1$ and $Le = 1$, i.e. the differential-diffusion-induced heat release variations are contained in this reduced representation of the local mixture state. The coupling between (ϕ, h, Y_H) and the third-level (kinematic) parameters $(\kappa, |\nabla T|)$ as well as the role of external effects (e.g. turbulence, cf. Fig. 2), will be analyzed in Part II of the present study [1].

Table 5: Irreducible error intrinsic to heat release rate predictions from different input parameter sets (normalized by the temperature-based error value computed from the $Le = 1$ flame). Data in parentheses corresponds to the $Le = 1$ flame.

Parameter Set Π	$\epsilon_{Le>1}^2(\Pi) / \epsilon_{Le=1}^2(T)$
T	5.49 (1.00)
T, Y_H	1.84 (0.59)
T, Y_{H_2}	0.93 (0.53)
T, Y_{H_2}, Y_H	0.54 (0.35)
T, h	1.88
T, h, Y_H	1.07
T, h, Y_{H_2}	0.77
T, ϕ	0.94 (0.54)
T, ϕ, Y_H	0.50
T, ϕ, Y_{H_2}	0.76
T, ϕ, h	0.64
T, ϕ, h, Y_{H_2}	0.55
T, ϕ, h, Y_H	0.30 (0.31)
T, κ	3.84 (0.69)
$T, \nabla T $	1.78 (0.74)
$T, \nabla T , \kappa$	1.52
T, a_t	4.68 (0.93)
T, κ, a_t	3.46 (0.59)
$T, \nabla T , a_t$	1.52
$T, \kappa, \nabla T , a_t$	1.35
$T, \kappa, \nabla T , \frac{1}{ \nabla T } \frac{D_T(\nabla T)}{D_T(t)}$	1.36

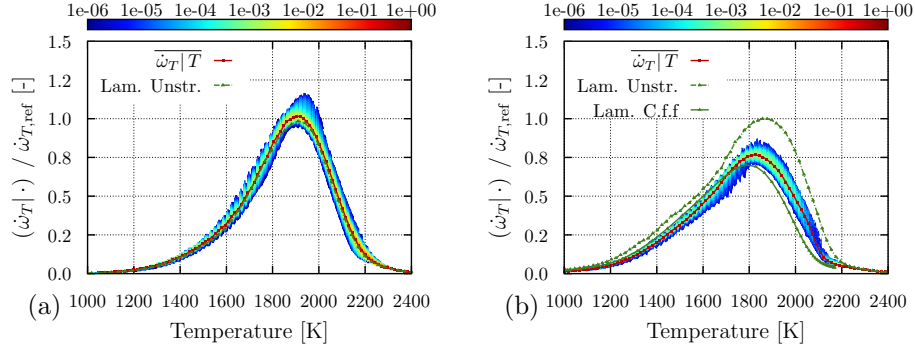


Figure 7: Planar Flame: Joint-PDFs of heat release rate and temperature for the $Le = 1$ dataset (a) and the engine-relevant $Le > 1$ flame (b) at $t = 2.8 \tau_t$. Different from Fig. 6, all data has been conditioned on $(\langle \phi | T \rangle, \langle h | T \rangle, \langle Y_H | T \rangle)$. The reduced variance in sub-figure (b) compared to Fig. 6 (b) illustrates that heat release variations due to differential diffusion effects are contained in these three parameters.

As a final note on the selection of suitable marker species, it should be mentioned that for a given Y_{H_2} as a representative parameter for ϕ , there is some correlation between $|\nabla T|$ (or χ) and Y_H (cf. Fig A.1 (b)), which according to Fig. 2 may explain the low irreducible error observed for the parameter set (T, Y_{H_2}, Y_H) .

The preceding empirical parameter tests based on the parametric representation of the governing flame physics shown in Fig. 2 lead in fact to similar parameters on the third and fourth level as previously derived from the premixed flamelet equations by Savard and Blanquart [84]. In the unity Lewis number limit, the scalar dissipation rate $\chi_c = 2D_{th} |\nabla c|^2$ was shown to be the only parameter in the flamelet equations, while for non-unity-Lewis-number flames, the diffusion rate of the progress variable $\xi_c = \frac{\partial}{\partial x_j} \left(\rho D_{th} \frac{\partial c}{\partial x_j} \right)$ occurs as additional parameter. To relate the present findings to the optimal estimator tests performed by Savard and Blanquart, the following decomposition

of the diffusion rate of the progress variable ζ (cf. Eq. (6)) is considered:

$$\begin{aligned}\xi_\zeta &= \frac{\partial}{\partial x_j} \left(\rho D_{\text{th}} \frac{\partial \zeta}{\partial x_j} \right) = -\rho D_{\text{th}} |\nabla \zeta| \kappa_\zeta - \frac{\partial}{\partial x_n} (\rho D_{\text{th}} |\nabla \zeta|) \\ &= \xi_{\zeta, \kappa} + \xi_{\zeta, n}.\end{aligned}\tag{11}$$

Note that in contrast to the results presented in Tab. 5, ζ is used here since diffusive transport is entirely contained in ξ_ζ , which is not the case for temperature. From Eq. (11), it can already be concluded that the tested parameter set $(T, |\nabla \zeta|, \kappa_\zeta)$ (or $(T, |\nabla T|, \kappa)$ in Tab. 5) essentially represents $\xi_{\zeta, \kappa}$, while $\xi_{\zeta, n}$ has not yet been tested for the present datasets. In Tab. 6, optimal estimator results are shown for the third-level parameters known from Tab. 5, but expressed in terms of gradients of ζ and complemented by $\xi_{\zeta, \kappa}$ and $\xi_{\zeta, n}$. Overall, the trends observed in Tab. 5 hold for the progress variable as well, and the low irreducible error shown for $(T, |\nabla \zeta|, \xi_{\zeta, \kappa}, \xi_{\zeta, n})$ confirms the effectiveness of the parameter combination χ_c and ξ_c , which was derived and tested for non-unity-Lewis-number flames by Savard and Blanquart [84]. It should be noted that a strong correlation between the local heat release rate and ξ_ζ can be expected from Eq. (6), since the chemical source term is entirely balanced by the diffusion rate. Instead, the flame structure and geometry have been parameterized by $|\nabla \zeta|$ and κ_ζ in the present study, since the transport equations for both quantities highlight dependencies on external effects such as hydrodynamic strain. Replacing $(|\nabla \zeta|, \kappa_\zeta)$ by $(|\nabla \zeta|, \xi_{\zeta, \kappa})$ gives almost identical irreducible errors, as shown in Tab. 6. However, the effectiveness of $\xi_{\zeta, n}$ in reducing the irreducible error suggests to analyze the role of external effects on this term in more detail in the future.

In order to use the results provided in Tab. 5 or 6 for the design of a

Table 6: Irreducible error intrinsic to heat release rate predictions from different input parameter sets (normalized by the temperature-based error value computed from the $Le = 1$ flame), similar to the study by Savard and Blanquart [84]. ξ is defined in Eq. (11). Data in parentheses corresponds to the $Le = 1$ flame.

Parameter Set Π	$\epsilon_{Le>1}^2(\Pi) / \epsilon_{Le=1}^2(T)$
T, κ_ζ	4.23
$T, \nabla\zeta $	1.64 (0.63)
$T, \nabla\zeta , \kappa_\zeta$	1.38
$T, \nabla\zeta , \xi_{\zeta,\kappa}$	1.37
$T, \nabla\zeta , \xi_{\zeta,n}$	1.17
$T, \nabla\zeta , \kappa_\zeta, \xi_{\zeta,n}$	0.93
$T, \nabla\zeta , \xi_{\zeta,\kappa}, \xi_{\zeta,n}$	0.92

reduced-order chemistry model, e.g. based on flamelet generated manifolds (FGM) [85], several additional considerations will be necessary. The preceding analysis may be considered as a first step that resulted in quantitative criteria for selecting a viable parameterization for the heat-release-rate response to differential diffusion from the tested parameter set candidates. Additionally, the control variable space to be selected should provide a unique mapping to the FGM, which would need to be assessed in a second step. Knudsen et al. [59] tested several control variable candidates in this regard and identified non-unique mapping as an issue for the parameters Y_{H_2} , Y_{CO} (first-level), as well as the scalar dissipation rate χ_c (third-level) in a strained methane/air flame, particularly at high strain rates. Third, the (conditional) controlling variables or relevant statistical moments need to be determined from the reacting flow simulation (DNS, LES, RANS), which may introduce

a need for additional closure models and numerical methods. In this respect, it will be more challenging to develop a model that, e.g. relies on a transport equation for χ_c (third-level) [86] than using a transport equation for mixture fraction (representative for local equivalence ratio, second-level) [87, 88], or tracking a species mass fraction such as Y_H (first-level) [59]. For LES, χ_c may instead be computed from an eddy-diffusivity-based time scale and an appropriately modeled subfilter scalar variance, in analogy to previous work on non-premixed combustion modeling [89]. In previous modeling studies on stretched premixed flames, the FGM was typically extended by one additional controlling variable in order to account for differential diffusion effects. Regarding first-level parameters, Y_{CO} [64], Y_{OH} [90] and Y_H [59] were considered, but mainly in methane/air flames with effective Lewis numbers close to unity. As shown in this study, for modeling of flames with Lewis numbers significantly different from unity, (additionally) selecting a species that correlates with the local equivalence ratio might be more suitable. Second-level parameters were mostly used for laminar [87] or resolved-turbulence simulations [55, 88] with reduced chemistry parameterized by mixture fraction or a combination of element mass fractions. Here, it should be noted that changes in element mass fraction and enthalpy may decouple, i.e. require more than one additional FGM controlling variable at high-stretch conditions [64]. Concerning third-level parameters, χ_c was used in RANS [91] and LES [92] studies. With respect to fourth-level parameters it should be noted that the addition of a dynamic parameter in the optimal estimator analysis was motivated by capturing transient effects, which are not covered by steady FGM approaches per se. Additionally, the dynamic parameter would

need to be unambiguously defined in turbulent and canonical laminar flame configurations [59].

To finally connect the presented macroscopic and micro-scale analyses, the correlation between the local mixture state parameters h and ϕ with $\bar{I}_{0,\text{rn}}$ (cf. Fig. 3 (a)) during flame development will be briefly discussed hereafter. For the purpose of this analysis, both h and ϕ have been averaged over the reaction zones of the $Le > 1$ flames. The time evolution of both parameters and $\bar{I}_{0,\text{rn}}$ is shown in Fig. 8. For the planar flame configuration, $\bar{I}_{0,\text{rn}}$ almost exactly follows the history of the normalized reaction zone enthalpy. Here, the reference enthalpy for normalization was obtained by applying the reaction zone averaging in an unstretched laminar flame. In the flame kernel configuration, the initial decrease of reaction zone enthalpy from the initial conditions due to the development of differential diffusion effects observed in the planar flame is effectively delayed by spark ignition. While the flame kernel stretch factor qualitatively follows the normalized reaction zone enthalpy evolution, both lines deviate significantly. This is likely due to the lean mixture conditions that rapidly develop inside the reaction zone of the flame kernel (cf. Fig. 8 (b)). At $t \approx 0.55 \tau_t$, $\bar{I}_{0,\text{rn}}$ is approximately equal in both flame configurations. At this time instant, the flame kernel exhibits noticeable excess enthalpy, but substantially leaner mixture inside the reaction zone as compared to the planar flame. When the ignition enthalpy decays, the burning velocity of the flame kernel reaches a minimum and then slowly recovers, in line with the mixture state as the positive global mean curvature reduces during flame kernel growth.

Since small flame kernels are particularly sensitive to external perturba-

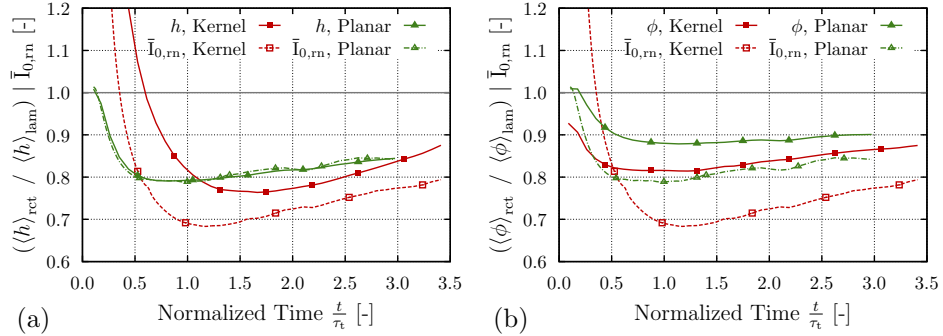


Figure 8: Reaction-zone-averaged enthalpy (a) and local equivalence ratio (b) compared to the reaction/normal diffusion stretch factor $\bar{I}_{0,rn}$ as function of time for $Le > 1$. Note that both h and ϕ are approximately constant in $Le = 1$ flames.

tions, the reduction in burning velocity (cf. Fig. 3 (a)) caused by low enthalpy and equivalence ratio inside the reaction zone in $Le > 1$ mixtures is critical in terms of CCV in engines. However, systematic development of an appropriate spark ignition strategy may enable effective counter measures. From laminar investigations it is known that the minimum ignition energy (MIE) increases with increasing Lewis number [93, 94], which is in line with the present turbulent flame results.

Conclusions

The intention of the present work is to clarify the role of differential diffusion during early flame kernel development in the thin reaction zones regime. Due to the expected relevance for the occurrence of cycle-to-cycle variations in SI engines, a DNS database has been carefully designed to be representative of practical engine conditions. Conclusive analyses were enabled by systematic variations of the global flame geometry and the mixture Lewis number of a realistic transportation fuel and air. A macroscopic analysis of

the global burning rate as practical quantity of interest has shown the impact of differential diffusion during early flame kernel development. Further, the local heat release rate response has been used as starting point for a systematic micro-scale analysis on the complex parameter dependencies inside the turbulent flame structure. Specifically, the following conclusions can be drawn:

- The detrimental effect of differential diffusion on the net burning rate of flame kernels with fuel $Le > 1$ is mainly due to changes in the normal propagation velocity, while differences in flame area at the same flame radius are slightly less important, though still significant under the present conditions. This is in agreement with the findings of Dinesh et al. [27] in flames with $Le < 1$. However, the observation that the flame-area dependence on thermal-diffusive effects is weakened under high-Reynolds-number flow conditions [27] may not translate to the very early phase of flame kernel development, which is a topic suggested for future work.
- Early flame kernel area growth is significantly reduced in the $Le > 1$ flame, which has been attributed to a reduction in the normal-propagation term in the surface area evolution equation. Area production by propagation of the curved flame surface is proportional to the normal-propagation stretch factor $\bar{I}_{0,rm}$, which has been shown to strongly suffer from low enthalpy and local equivalence ratio levels inside the reaction zone as a consequence of differential diffusion. Under the present turbulent conditions, differential diffusion thus acts on initial flame area growth in a very similar way as known from laminar spherical flames.

- Non-unity Lewis numbers were shown to result in strong variations in local heat release rate. In particular, very low heat release rates were locally observed. This is in agreement with results reported by Shim et al. [70] for H_2 /air flames located in the thin reaction zones regime. However, such locally low heat release rates were neither observed under flame conditions in the corrugated flamelets regime by Shim et al., nor in the present $\text{Le} = 1$ datasets in the thin reaction zones regime. Hence, heat release fluctuations seem to be particularly pronounced in $\text{Le} \neq 1$ flames located in the thin reaction zones regime. Both of these conditions are typically found in SI engines. The present results on iso-octane/air flames are in agreement with previous work on higher hydrocarbon fuels [66, 71].
- By using the optimal estimator concept, the fluctuations in heat release rate for a given temperature (or progress variable) have been quantitatively attributed to different parameter dependencies and related to the behavior of a $\text{Le} = 1$ flame. Specifically, a hierarchical grouping of parameter sets based on coupling-strength with the quantity of interest (heat release rate) has been proposed, i.e. first-level (temperature and species mass fractions, reaction/diffusion-controlled), second-level (equivalence ratio and enthalpy, diffusion-controlled), third-level (curvature and scalar gradient magnitude, kinematic) and fourth-level (tangential strain as a measure for time-rate-of-change of third-level parameters, kinematic/dynamic) parameters. On each level, a dominant parameter can be identified (cf. Tab. 5), which may be useful for modeling purposes. For the present analysis, the objective was to find a

reduced representation of the local mixture state, which determines the heat release rate. It turned out that conditioning on the parameter set (T, ϕ, h, Y_H) reduces the remaining scatter around the conditional mean heat release rate to identical levels in both $Le > 1$ and $Le = 1$ flames, which is in agreement with the proposed flame physics schematic based on findings from literature (cf. Fig. 2).

The coupled nature of the local mixture state with the flame geometry and structure due to differential diffusion is discussed in Part II of the present study [1].

Acknowledgement

The authors from RWTH Aachen University gratefully acknowledge partial funding by Honda R&D and by the Deutsche Forschungsgemeinschaft (DFG, German Research Foundation) under Germany's Excellence Strategy - Exzellenzcluster 2186 'The Fuel Science Center' ID: 390919832.

The authors gratefully acknowledge the Gauss Centre for Supercomputing e.V. (www.gauss-centre.eu) for funding this project by providing computing time on the GCS Supercomputer Super-MUC at Leibniz Supercomputing Centre (LRZ, www.lrz.de).

Data analyses were performed with computing resources granted by RWTH Aachen University under project thes0373.

S.K. gratefully acknowledges financial support from the National Research Foundation of Korea (NRF) grant by the Korea government (MSIP) (No. 2017R1A2B3008273).

T.F. would like to thank Günter Paczko, sadly no longer with us, for the helpful discussions in all these years.

Appendix A. Correlation between Marker Species and Mixture State Parameters

The optimal estimator results presented in Tab. 5 suggest to parameterize the local mixture state with the quantities (ϕ, h, Y_{H}) for a given temperature. Further, some parameters that were assigned to different hierarchical groups in fact showed similar performance. Specifically, the first-level parameter set (T, Y_{H_2}) was shown to yield an almost identical irreducible error as the second-level parameter set (T, ϕ) . Similarly, the first-level parameter set (T, Y_{H}) and the third-level parameter set $(T, |\nabla T|)$ yielded comparable irreducible errors. Here, the correlation of these marker species with the representative mixture state (ϕ) and flame structure $(|\nabla T|)$ parameters shall be assessed. The joint-PDFs shown in Fig. A.1 confirm a correlation between ϕ and Y_{H_2} for a given temperature and fixed Y_{H} , as well as a correlation between $|\nabla T|$ and Y_{H} for a given temperature and fixed Y_{H_2} . Hence, Y_{H_2} can be considered as a marker for the differential-diffusion effect on the local mixture composition, while Y_{H} may contain information on the local mixture internal energy distribution caused by changes in flame structure (cf. Fig. 2).

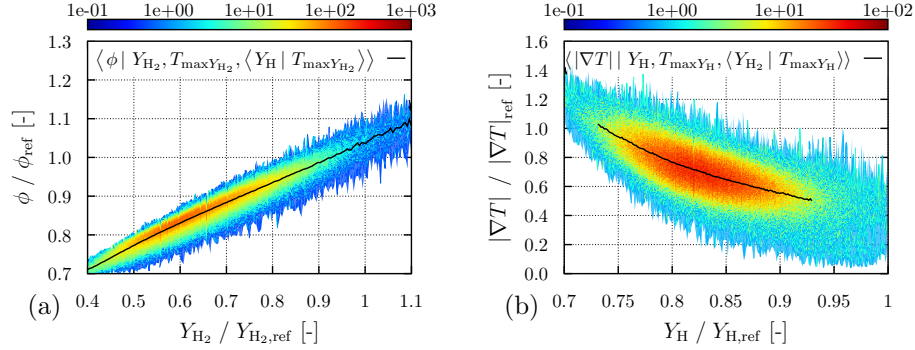


Figure A.1: Planar Flame: Joint-PDF of the local equivalence ratio ϕ conditioned on $(T = T_{\text{max}Y_{\text{H}_2}}, \langle Y_{\text{H}} | T = T_{\text{max}Y_{\text{H}_2}} \rangle)$ and the mass fraction of molecular hydrogen Y_{H_2} (a); of the temperature gradient magnitude $|\nabla T|$ conditioned on $(T = T_{\text{max}Y_{\text{H}}}, \langle Y_{\text{H}_2} | T = T_{\text{max}Y_{\text{H}}} \rangle)$ and the H-radical mass fraction Y_{H} . Here, the data have been conditioned on temperature iso-surfaces corresponding to the maximum species mass fraction in the laminar unstretched flame.

References

- [1] T. Falkenstein, H. Chu, M. Bode, S. Kang, H. Pitsch, The role of differential diffusion during early flame kernel development under engine conditions - Part II: The effect of flame geometry and structure, Submitted to Combustion and Flame (2019)arXiv:1910.10150.
- [2] P. Aleiferis, A. Taylor, K. Ishii, Y. Urata, The nature of early flame development in a lean-burn stratified-charge spark-ignition engine, Combustion and Flame 136 (3) (2004) 283–302.
- [3] D. Jung, K. Sasaki, N. Iida, Effects of increased spark discharge energy and enhanced in-cylinder turbulence level on lean limits and cycle-to-cycle variations of combustion for SI engine operation, Applied Energy 205 (2017) 1467–1477.

- [4] E. E. Milkins, H. C. Watson, L. C. Goldsworthy, R. J. Hallworth, Cycle by cycle variability in emissions of a spark ignition engine, in: International Automobile Engineering and Manufacturing Meeting, SAE International, 1974.
- [5] A. Karvountzis-Kontakiotis, A. Dimaratos, L. Ntziachristos, Z. Samaras, Exploring the stochastic and deterministic aspects of cyclic emission variability on a high speed spark-ignition engine, *Energy* 118 (2017) 68–76.
- [6] M. Drake, D. Haworth, Advanced gasoline engine development using optical diagnostics and numerical modeling, *Proceedings of the Combustion Institute* 31 (1) (2007) 99–124.
- [7] R. Maly, State of the art and future needs in S.I. engine combustion, *Symposium (International) on Combustion* 25 (1) (1994) 111–124.
- [8] P. Schiffmann, D. L. Reuss, V. Sick, Empirical investigation of spark-ignited flame-initiation cycle-to-cycle variability in a homogeneous charge reciprocating engine, *International Journal of Engine Research* 19 (5) (2018) 491–508.
- [9] R. Abdel-Gayed, D. Bradley, M. Hamid, M. Lawes, Lewis number effects on turbulent burning velocity, *Symposium (International) on Combustion* 20 (1) (1985) 505–512.
- [10] K. T. Aung, M. I. Hassan, S. Kwon, L. K. Tseng, O. C. Kwon, G. M. Faeth, Flame/stretch interactions in laminar and turbulent premixed flames, *Combustion Science and Technology* 174 (1) (2002) 61–99.

- [11] A. Saha, S. Chaudhuri, C. K. Law, Flame surface statistics of constant-pressure turbulent expanding premixed flames, *Physics of Fluids* 26 (4) (2014) 045109.
- [12] P. Brequigny, F. Halter, C. Mounam-Rousselle, Lewis number and Markstein length effects on turbulent expanding flames in a spherical vessel, *Experimental Thermal and Fluid Science* 73 (2016) 33–41.
- [13] K. Jenkins, R. Cant, Curvature effects on flame kernels in a turbulent environment, *Proceedings of the Combustion Institute* 29 (2) (2002) 2023–2029.
- [14] D. Thévenin, Three-dimensional direct simulations and structure of expanding turbulent methane flames, *Proceedings of the Combustion Institute* 30 (1) (2005) 629–637.
- [15] M. Klein, N. Chakraborty, K. W. Jenkins, R. S. Cant, Effects of initial radius on the propagation of premixed flame kernels in a turbulent environment, *Physics of Fluids* 18 (5) (2006) 055102.
- [16] K. Jenkins, M. Klein, N. Chakraborty, R. Cant, Effects of strain rate and curvature on the propagation of a spherical flame kernel in the thin-reaction-zones regime, *Combustion and Flame* 145 (1) (2006) 415–434.
- [17] N. Chakraborty, E. Mastorakos, R. S. Cant, Effects of turbulence on spark ignition in inhomogeneous mixtures: A direct numerical simulation (DNS) study, *Combustion Science and Technology* 179 (1-2) (2007) 293–317.

- [18] N. Chakraborty, M. Klein, R. Cant, Stretch rate effects on displacement speed in turbulent premixed flame kernels in the thin reaction zones regime, *Proceedings of the Combustion Institute* 31 (1) (2007) 1385–1392.
- [19] R. J. M. Bastiaans, J. A. van Oijen, L. P. H. de Goey, Analysis of a strong mass-based flame stretch model for turbulent premixed combustion, *Physics of Fluids* 21 (1) (2009) 015105.
- [20] N. Chakraborty, M. Klein, Effects of global flame curvature on surface density function transport in turbulent premixed flame kernels in the thin reaction zones regime, *Proceedings of the Combustion Institute* 32 (1) (2009) 1435–1443.
- [21] H. Shalaby, D. Thévenin, Statistically significant results for the propagation of a turbulent flame kernel using direct numerical simulation, *Flow, Turbulence and Combustion* 84 (3) (2010) 357–367.
- [22] T. Echekki, T. Poinso, T. Baritaud, A. Trouvé, Modeling and simulation of turbulent flame kernel evolution, *Tech. Rep. 41525*, Institut Français du Pétrole (1994).
- [23] T. D. Dunstan, K. W. Jenkins, The effects of hydrogen substitution on turbulent premixed methane-air kernels using direct numerical simulation, *International Journal of Hydrogen Energy* 34 (19) (2009) 8389–8404.
- [24] G. Fru, D. Thévenin, G. Janiga, Impact of turbulence intensity and

- equivalence ratio on the burning rate of premixed methane-air flames, *Energies* 4 (6) (2011) 878–893.
- [25] C. Pera, S. Chevillard, J. Reveillon, Effects of residual burnt gas heterogeneity on early flame propagation and on cyclic variability in spark-ignited engines, *Combustion and Flame* 160 (6) (2013) 1020–1032.
- [26] B. Yenerdag, N. Fukushima, M. Shimura, M. Tanahashi, T. Miyauchi, Turbulence-flame interaction and fractal characteristics of H₂-air premixed flame under pressure rising condition, *Proceedings of the Combustion Institute* 35 (2) (2015) 1277–1285.
- [27] K. R. Dinesh, H. Shalaby, K. Luo, J. van Oijen, D. Thévenin, High hydrogen content syngas fuel burning in lean premixed spherical flames at elevated pressures: Effects of preferential diffusion, *International Journal of Hydrogen Energy* 41 (40) (2016) 18231–18249.
- [28] H. A. Uranakara, S. Chaudhuri, K. Lakshmisha, On the extinction of igniting kernels in near-isotropic turbulence, *Proceedings of the Combustion Institute* 36 (2) (2017) 1793–1800.
- [29] N. Saito, Y. Minamoto, B. Yenerdag, M. Shimura, M. Tanahashi, Effects of turbulence on ignition of methane-air and n-heptane-air fully premixed mixtures, *Combustion Science and Technology* 190 (3) (2018) 452–470.
- [30] A. Alqallaf, M. Klein, N. Chakraborty, Effects of Lewis number on the evolution of curvature in spherically expanding turbulent premixed flames, *Fluids* 4 (1).

- [31] E. R. Hawkes, J. H. Chen, Direct numerical simulation of hydrogen-enriched lean premixed methane-air flames, *Combustion and Flame* 138 (3) (2004) 242–258.
- [32] B. Savard, S. Lapointe, A. Teodorczyk, Numerical investigation of the effect of pressure on heat release rate in iso-octane premixed turbulent flames under conditions relevant to SI engines, *Proceedings of the Combustion Institute* 36 (3) (2017) 3543–3549.
- [33] A. Aspden, J. Bell, M. Day, F. Egolfopoulos, Turbulence-flame interactions in lean premixed dodecane flames, *Proceedings of the Combustion Institute* 36 (2) (2017) 2005–2016.
- [34] A. Aspden, M. Day, J. Bell, Three-dimensional direct numerical simulation of turbulent lean premixed methane combustion with detailed kinetics, *Combustion and Flame* 166 (2016) 266–283.
- [35] T. Falkenstein, S. Kang, L. Cai, M. Bode, H. Pitsch, DNS study of the global heat release rate during early flame kernel development under engine conditions, *Combustion and Flame* 213 (2020) 455–466.
- [36] T. Falkenstein, S. Kang, H. Pitsch, Analysis of premixed flame kernel/turbulence interactions under engine conditions based on direct numerical simulation data, *Journal of Fluid Mechanics* 885 (2020) A32.
- [37] K. N. C. Bray, Studies of the turbulent burning velocity, *Proceedings of the Royal Society of London A: Mathematical, Physical and Engineering Sciences* 431 (1882) (1990) 315–335.

- [38] M. Boger, D. Veynante, H. Boughanem, A. Trouvé, Direct numerical simulation analysis of flame surface density concept for large eddy simulation of turbulent premixed combustion, *Symposium (International) on Combustion* 27 (1) (1998) 917–925.
- [39] T. Echekki, J. Chen, Analysis of the contribution of curvature to premixed flame propagation, *Combustion and Flame* 118 (1999) 308–311.
- [40] S. M. Candel, T. J. Poinso, Flame stretch and the balance equation for the flame area, *Combustion Science and Technology* 70 (1-3) (1990) 1–15.
- [41] S. H. Kim, H. Pitsch, Scalar gradient and small-scale structure in turbulent premixed combustion, *Physics of Fluids* 19 (11) (2007) 115104.
- [42] R. Sankaran, E. R. Hawkes, J. H. Chen, T. Lu, C. K. Law, Structure of a spatially developing turbulent lean methane-air bunsen flame, *Proceedings of the Combustion Institute* 31 (1) (2007) 1291–1298.
- [43] S. B. Pope, The evolution of surfaces in turbulence, *International Journal of Engineering Science* 26 (1988) 445–469.
- [44] C. Dopazo, J. Martin, L. Cifuentes, J. Hierro, Strain, rotation and curvature of non-material propagating iso-scalar surfaces in homogeneous turbulence, *Flow, Turbulence and Combustion* 101 (1) (2018) 1–32.
- [45] P. Clavin, F. A. Williams, Effects of molecular diffusion and of thermal expansion on the structure and dynamics of premixed flames in turbulent flows of large scale and low intensity, *Journal of Fluid Mechanics* 116 (1982) 251–282.

- [46] M. Matalon, B. J. Matkowsky, Flames as gasdynamic discontinuities, *Journal of Fluid Mechanics* 124 (1982) 239–259.
- [47] N. Peters, *Turbulent Combustion*, Cambridge Monographs on Mechanics, Cambridge University Press, 2000.
- [48] F. Williams, Progress in knowledge of flamelet structure and extinction, *Progress in Energy and Combustion Science* 26 (4) (2000) 657–682.
- [49] D. Linse, C. Hasse, B. Durst, An experimental and numerical investigation of turbulent flame propagation and flame structure in a turbo-charged direct injection gasoline engine, *Combustion Theory and Modelling* 13 (1) (2009) 167–188.
- [50] J. Heywood, Combustion and its modeling in spark-ignition engines, in: *Proceedings of the Third International Symposium on Diagnostics and Modeling of Combustion in Internal Combustion Engines (COMODIA)*, Yokohama, Japan, July 11 - 14, 1994, pp. 1–15.
- [51] D. Heim, J. Ghandhi, A detailed study of in-cylinder flow and turbulence using PIV, *SAE International Journal of Engines* 4 (1) (2011) 1642–1668.
- [52] R. Hilbert, F. Tap, H. El-Rabii, D. Thévenin, Impact of detailed chemistry and transport models on turbulent combustion simulations, *Progress in Energy and Combustion Science* 30 (1) (2004) 61–117.
- [53] H. Pitsch, N. Peters, Numerical and asymptotic studies of the structure of premixed iso-octane flames, *Symposium (International) on Combustion* 26 (1996) 763–771.

- [54] J. O. Hirschfelder, C. F. Curtiss, R. B. Bird, Molecular theory of gases and liquids, Vol. 17, John Wiley and Sons, New York, 1954.
- [55] J. van Oijen, A. Donini, R. Bastiaans, J. ten Thije Boonkamp, L. de Goey, State-of-the-art in premixed combustion modeling using flamelet generated manifolds, Progress in Energy and Combustion Science 57 (2016) 30–74.
- [56] B. Müller, Low-mach-number asymptotics of the Navier-Stokes equations, Journal of Engineering Mathematics 34 (1) (1998) 97–109.
- [57] H. Pitsch, A C++ computer program for 0d and 1d laminar flame calculations (1998).
URL <https://www.itv.rwth-aachen.de/index.php?id=flamemaster>
- [58] D. M. Smooke, J. A. Miller, R. J. Kee, Determination of adiabatic flame speeds by boundary value methods, Combustion Science and Technology 34 (1-6) (1983) 79–90.
- [59] E. Knudsen, H. Kolla, E. R. Hawkes, H. Pitsch, LES of a premixed jet flame DNS using a strained flamelet model, Combustion and Flame 160 (12) (2013) 2911–2927.
- [60] P. Trisjono, K. Kleinheinz, E. R. Hawkes, H. Pitsch, Modeling turbulence-chemistry interaction in lean premixed hydrogen flames with a strained flamelet model, Combustion and Flame 174 (2016) 194–207.
- [61] G. Dixon-Lewis, T. David, P. Gaskell, S. Fukutani, H. Jinno, J. Miller, R. Kee, M. Smooke, N. Peters, E. Effelsberg, J. Warnatz, F. Behrendt,

- Calculation of the structure and extinction limit of a methane-air counterflow diffusion flame in the forward stagnation region of a porous cylinder, *Symposium (International) on Combustion* 20 (1) (1985) 1893–1904.
- [62] U. Maas, B. Raffel, J. Wolfrum, J. Warnatz, Observation and simulation of laser induced ignition processes in O_2-O_3 and H_2-O_2 mixtures, *Symposium (International) on Combustion* 21 (1) (1988) 1869–1876.
- [63] L. Petzold, Description of DASSL: a differential/algebraic system solver.
- [64] J. A. van Oijen, L. P. H. de Goey, Modelling of premixed counterflow flames using the flamelet-generated manifold method, *Combustion Theory and Modelling* 6 (3) (2002) 463–478.
- [65] A. Lipatnikov, J. Chomiak, Molecular transport effects on turbulent flame propagation and structure, *Progress in Energy and Combustion Science* 31 (1) (2005) 1–73.
- [66] B. Savard, G. Blanquart, Broken reaction zone and differential diffusion effects in high Karlovitz $n-C_7H_{16}$ premixed turbulent flames, *Combustion and Flame* 162 (5) (2015) 2020–2033.
- [67] D. C. Haworth, T. J. Poinso, Numerical simulations of Lewis number effects in turbulent premixed flames, *Journal of Fluid Mechanics* 244 (1992) 405–436.
- [68] A. Trouvé, T. Poinso, The evolution equation for the flame surface density in turbulent premixed combustion, *Journal of Fluid Mechanics* 278 (1994) 1–31.

- [69] J. B. Bell, R. K. Cheng, M. S. Day, I. G. Shepherd, Numerical simulation of Lewis number effects on lean premixed turbulent flames, *Proceedings of the Combustion Institute* 31 (1) (2007) 1309–1317.
- [70] Y.-S. Shim, N. Fukushima, M. Shimura, Y. Nada, M. Tanahashi, T. Miyauchi, Radical fingering in turbulent premixed flame classified into thin reaction zones, *Proceedings of the Combustion Institute* 34 (1) (2013) 1383–1391.
- [71] S. Lapointe, B. Savard, G. Blanquart, Differential diffusion effects, distributed burning, and local extinctions in high Karlovitz premixed flames, *Combustion and Flame* 162 (9) (2015) 3341–3355.
- [72] A. Moreau, O. Teytaud, J. P. Bertoglio, Optimal estimation for large-eddy simulation of turbulence and application to the analysis of subgrid models, *Physics of Fluids* 18 (10) (2006) 105101.
- [73] P. Trisjono, H. Pitsch, Systematic analysis strategies for the development of combustion models from DNS: A review, *Flow, Turbulence and Combustion* 95 (2) (2015) 231–259.
- [74] L. Berger, K. Kleinheinz, A. Attili, F. Bisetti, H. Pitsch, M. E. Mueller, Numerically accurate computational techniques for optimal estimator analyses of multi-parameter models, *Combustion Theory and Modelling* 22 (3) (2018) 480–504.
- [75] D. Dasgupta, W. Sun, M. Day, T. Lieuwen, Effect of turbulence-chemistry interactions on chemical pathways for turbulent hydrogen-air premixed flames, *Combustion and Flame* 176 (2017) 191–201.

- [76] D. Dasgupta, W. Sun, M. Day, A. Aspden, T. Lieuwen, Investigation of turbulence effects on chemical pathways for n-dodecane, in: AIAA Aerospace Sciences Meeting, Kissimmee, FL, 8–12 January, 2018.
- [77] L. de Goey, J. ten Thijsse Boonkamp, A flamelet description of premixed laminar flames and the relation with flame stretch, *Combustion and Flame* 119 (3) (1999) 253–271.
- [78] C. J. Pope, R. A. Shandross, J. B. Howard, Variation of equivalence ratio and element ratios with distance from burner in premixed one-dimensional flames, *Combustion and Flame* 116 (4) (1999) 605–614.
- [79] W. T. Ashurst, N. Peters, M. D. Smooke, Numerical simulation of turbulent flame structure with non-unity Lewis number, *Combustion Science and Technology* 53 (4-6) (1987) 339–375.
- [80] T. Echekki, J. H. Chen, Unsteady strain rate and curvature effects in turbulent premixed methane-air flames, *Combustion and Flame* 106 (1) (1996) 184–202.
- [81] J. B. Chen, H. G. Im, Stretch effects on the burning velocity of turbulent premixed hydrogen/air flames, *Proceedings of the Combustion Institute* 28 (1) (2000) 211–218.
- [82] N. Chakraborty, R. S. Cant, Influence of Lewis number on curvature effects in turbulent premixed flame propagation in the thin reaction zones regime, *Physics of Fluids* 17 (10) (2005) 105105.
- [83] B. Renou, A. Boukhalfa, D. Puechberty, M. Trinit, Effects of stretch on the local structure of freely propagating premixed low-turbulent flames

- with various Lewis numbers, Symposium (International) on Combustion 27 (1) (1998) 841–847.
- [84] B. Savard, G. Blanquart, Effects of dissipation rate and diffusion rate of the progress variable on local fuel burning rate in premixed turbulent flames, *Combustion and Flame* 180 (2017) 77–87.
- [85] J. van Oijen, L. de Goey, Modelling of premixed laminar flames using flamelet-generated manifolds, *Combustion Science and Technology* 161 (1) (2000) 113–137.
- [86] N. Swaminathan, K. Bray, Effect of dilatation on scalar dissipation in turbulent premixed flames, *Combustion and Flame* 143 (4) (2005) 549–565.
- [87] J. D. Regele, E. Knudsen, H. Pitsch, G. Blanquart, A two-equation model for non-unity lewis number differential diffusion in lean premixed laminar flames, *Combustion and Flame* 160 (2) (2013) 240–250.
- [88] J. Schlup, G. Blanquart, Reproducing curvature effects due to differential diffusion in tabulated chemistry for premixed flames, *Proceedings of the Combustion Institute* 37 (2) (2019) 2511–2518.
- [89] V. Raman, H. Pitsch, R. O. Fox, Hybrid large-eddy simulation/lagrangian filtered-density-function approach for simulating turbulent combustion, *Combustion and Flame* 143 (1) (2005) 56–78.
- [90] J. van Oijen, R. Bastiaans, L. de Goey, Low-dimensional manifolds in direct numerical simulations of premixed turbulent flames, *Proceedings of the Combustion Institute* 31 (1) (2007) 1377–1384.

- [91] H. Kolla, N. Swaminathan, Strained flamelets for turbulent premixed flames, i: Formulation and planar flame results, *Combustion and Flame* 157 (5) (2010) 943–954.
- [92] B. Thornber, R. Bilger, A. Masri, E. Hawkes, An algorithm for LES of premixed compressible flows using the conditional moment closure model, *Journal of Computational Physics* 230 (20) (2011) 7687–7705.
- [93] P. Tromans, R. Furzeland, An analysis of Lewis number and flow effects on the ignition of premixed gases, *Symposium (International) on Combustion* 21 (1) (1988) 1891–1897.
- [94] Z. Chen, M. P. Burke, Y. Ju, On the critical flame radius and minimum ignition energy for spherical flame initiation, *Proceedings of the Combustion Institute* 33 (1) (2011) 1219–1226.